FULL PAPER

Magnetic Resonance in Medicine 000:000–000 (2012)

In Vivo ^{31}P MR Spectroscopic Imaging of the Human Prostate at 7 T: Safety and Feasibility

Thiele Kobus,[1]* Andreas K. Bitz,[2,3] Mark J. van Uden,[1] Miriam W. Lagemaat,[1] Eva Rothgang,[4,5] Stephan Orzada,[2,3] Arend Heerschap,[1] and Tom W. J. Scheenen[1,2]

^{31}P MR spectroscopic imaging of the human prostate provides information about phosphorylated metabolites that could be used for prostate cancer characterization. The sensitivity of a magnetic field strength of 7 T might enable 3D ^{31}P MR spectroscopic imaging with relevant spatial resolution in a clinically acceptable measurement time. To this end, a ^{31}P endorectal coil was developed and combined with an eight-channel ^{1}H body-array coil to relate metabolic information to anatomical location. An extensive safety validation was performed to evaluate the specific absorption rate, the radiofrequency field distribution, and the temperature distribution of both coils. This validation consisted of detailed Finite Integration Technique simulations, confirmed by MR thermometry and B_1^+ measurements in a phantom and in vivo temperature measurements. The safety studies demonstrated that the presence of the ^{31}P endorectal coil had no influence on the specific absorption rate levels and temperature distribution of the external eight-channel ^{1}H array coil. To stay within a 10 g averaged local specific absorption rate of 10 W/kg, a maximum time-averaged input power of 33 W for the ^{1}H array coil was allowed. For transmitting with the ^{31}P endorectal coil, our safety limit of less than 1°C temperature increase in vivo during a 15-min MR spectroscopic imaging experiment was reached at a time-averaged input power of 1.9 W. With this power setting, a second in vivo measurement was performed on a healthy volunteer. Using adiabatic excitation, 3D ^{31}P MR spectroscopic imaging produced spectra from the entire prostate in 18 min with a spatial resolution of 4 cm^3. The spectral resolution enabled the separate detection of phosphocholine, phosphoethanolamine, inorganic phosphate, and other metabolites that could play an important role in the characterization of prostate cancer. Magn Reson Med 000:000–000, 2012. © 2012 Wiley Periodicals, Inc.

Key words: prostate; ^{31}P MR spectroscopic imaging; endorectal ^{31}P coil; safety validation

MR is increasingly being used in the diagnosis, localization, and staging of prostate cancer. Prostate cancer is characterized by a hypointense signal on T_2-weighted images. Unfortunately, more benign pathologies like benign prostatic hyperplasia and prostatitis also show this decreased signal intensity. Higher specificities for detection (1) and localization (2,3) of prostate cancer were obtained when proton MR spectroscopic imaging (^{1}H MRSI) was added to the reading of T_2-weighted images. The use of MRSI enables the detection of biochemical changes that are characteristic for certain diseases. ^{1}H MRSI has been used to discriminate noncancer tissue from cancer tissue in the prostate using the choline plus creatine to citrate ratio. In cancer tissue an increase in this ratio is observed compared to normal tissue in single institution studies (4–6) as well as in a multicenter setting (7).

Phosphorus spectroscopy enables detection of metabolites with phosphorus atoms, e.g., phosphocreatine (PCr), inorganic phosphate (Pi), the three phosphate groups of adenosine triphosphate (ATP), phosphomonoesters (PME), and phosphodiesters (PDE). In the early 1990s, in vivo phosphorus spectroscopy of the human prostate was pioneered with measurements that used an endorectal coil (8–11). Using merely the coil reception profile for localization, differences in the PME to PCr ratio, the PME to β-ATP ratio and PCr to β-ATP ratio were observed between normal and cancer tissue (9,10). These studies were performed on a 2-T system and in 10–30 min one spectrum of a volume between 1.5 and 3 cm^3 could be acquired. To obtain information from different parts of the prostate, the endorectal coil was repositioned between different acquisitions (9).

At a magnetic field strength of 7 T, the increased chemical shift difference between signals might enable detection of the individual resonances of PME, i.e., phosphoethanolamine (PE) and phosphocholine (PC), and PDE, i.e., glycerophosphoethanolamine and glycerophosphocholine. Detection of these individual resonances could improve prostate cancer characterization, e.g., in the assessment of aggressiveness. A significant correlation between the Gleason score, the histopathological measure for aggressiveness, and the glycerophosphocholine/PC ratio has been reported in prostate cancer samples (12). The increased magnetic field strength also results in a higher signal-to-noise ratio (13), which makes it possible to perform localized three-dimensional (3D) ^{31}P MR spectroscopic imaging at a relevant spatial resolution in a clinically acceptable measurement time with

[1]Department of Radiology, Radboud University Nijmegen Medical Centre, Nijmegen, The Netherlands.

[2]Erwin L. Hahn Institute for Magnetic Resonance Imaging, Essen, Germany.

[3]Department of Diagnostic and Interventional Radiology and Neuroradiology, University Hospital Essen, Essen, Germany.

[4]Pattern Recognition Laboratory, University Erlangen-Nuremberg, Erlangen, Germany.

[5]Center for Applied Medical Imaging, Siemens Corporate Research, Baltimore, Maryland, USA.

Grant sponsor: European Research Council under the European Community's Seventh Framework Programme (FP7/2007-2013); Grant number: 243115; Grant sponsor: Dutch Cancer Society; Grant number: KUN 2007/3971; Grant sponsor: German Federal Ministry of Education and Research (Bundesministerium für Bildung und Forschung); Grant number: BMBF 01EZ0716.

*Correspondence to: Thiele Kobus, M.Sc., Department of Radiology, Radboud University Nijmegen Medical Centre, Geert Grooteplein 10, 6500 HB Nijmegen, The Netherlands. E-mail: T.kobus@rad.umcn.nl

Received 27 May 2011; revised 19 December 2011; accepted 22 December 2011.

DOI 10.1002/mrm.24175
Published online in Wiley Online Library (wileyonlinelibrary.com).

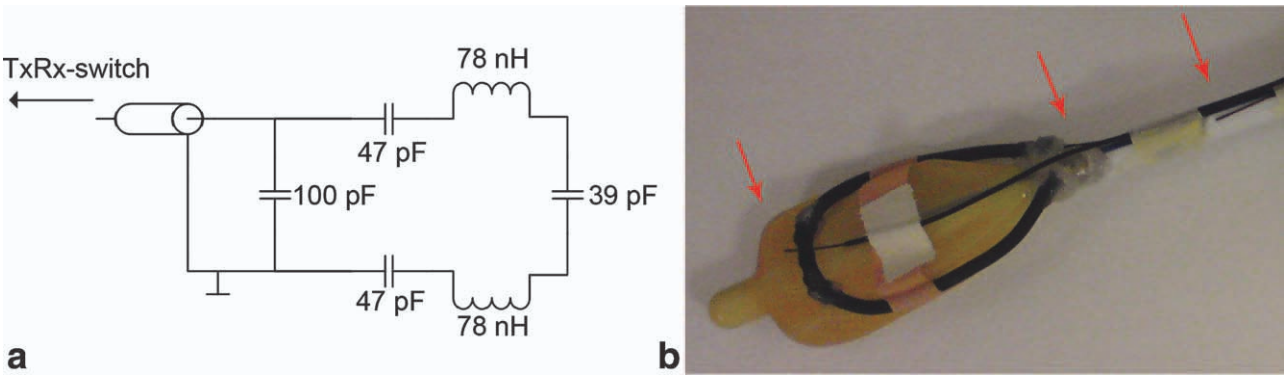

FIG. 1. **a:** Schematics of the electronic circuit of the ^{31}P TxRx endorectal coil. **b:** The ^{31}P TxRx endorectal coil without the outer balloon. The arrows indicate the location of the three fiber optic temperature sensors at the top of the coil, feed point, and coil wire to study the temperature increase in the phantom study. The coil loop has a length of 7.0 cm and a width of 3.7 cm. [Color figure can be viewed in the online issue, which is available at wileyonlinelibrary.com.]

a ^{31}P endorectal loop coil. To do so, ^{1}H MR imaging is necessary to relate the metabolic information to anatomy. When obtaining anatomical, T_2-weighted images of the abdomen at a field strength of 7 T severe inhomogeneities in the radiofrequency (RF) transmit field need to be overcome. Reaching refocusing flip angles in the center of the body at 7 T requires a significant amount of RF power, whereas the specific absorption rate (SAR) scales approximately with the square of the field strength. So, the increased RF power demand and RF transmit inhomogeneity is opposed by restrictions in RF power deposition with SAR limits, requiring the development of new coils and methods that enable a more efficient RF excitation.

Previously, Metzger et al. described a method to image the prostate at 7 T using multitransmit coils and RF shimming (14). The phase of the different coil elements was adjusted to obtain maximal B_1^+ coherence at the location of the prostate. When combining an eight-channel ^{1}H transmit/receive (TxRx) coil setup with a ^{31}P endorectal TxRx loop coil, RF coupling between the eight-channel coil elements and the ^{31}P endorectal coil needs to be investigated. The RF wavelength of the ^{1}H frequency in biological tissues at 7 T is ~12 cm. With these wavelengths, the ^{31}P prostate coil and cables might interfere with the eight-channel ^{1}H coil. This coupling could lead to inhomogeneous flip angle distributions and increased local SAR levels. If coupling exists between the coils or cables, this should be prevented or at least it should be ensured that the SAR stays within safe limits and that the images are not affected by an unpredictable B_1^+ distribution.

In this feasibility study, we dealt with all prerequisites for a setup that combines an eight-channel TxRx ^{1}H coil with a ^{31}P TxRx endorectal coil to study phosphorus metabolites in the prostate. The safety limits at our institution are based on the International Electrotechnical Commission (IEC) 60601-2-33 (Edition 3.0) safety guidelines (15). These state, as limits for local coils at normal operating level, a maximum time-averaged SAR of 10 W/kg or a maximum local tissue temperature of 39°C. As the body temperature of volunteers and patients in general is not measured before an MR exam, an input power leading to a maximum local increase of 1°C was used in this study as a safety limit. To assess compliance with these limits, Finite Integration Technique (FIT) simulations of both coils as well as their combination were performed to study the RF, SAR, and temperature distribution. From the simulations, the locations of the highest SAR deposition and temperature increase could be obtained, and these were validated by phantom measurements providing B_1^+ and temperature maps. Finally, in vivo temperature measurements were performed, by placing temperature probes on the ^{31}P endorectal coil at the positions with the highest determined power losses. From the simulations, phantom studies and in vivo measurements, the maximum input power to comply with the safety guidelines for transmitting with the ^{31}P endorectal coil and eight-channel ^{1}H array coil could be derived. In vivo measurements in compliance with the safety limits were performed using adiabatic excitation, and phosphorus spectra were obtained from the entire prostate and surrounding tissue with high spatial resolution (4 cm^3) in a single measurement.

METHODS

Hardware

^{31}P TxRx Endorectal Coil and Interface

The mechanical housing and conductors of an inflatable ^{1}H receive endorectal coil for use at 3 T (MEDRAD, Pittsburgh, PA) was used for the design of the ^{31}P TxRx endorectal coil. The coil was tuned and matched to 50 Ω at 120.3 MHz using small ceramic capacitors (American Technical Ceramics, Huntington Station, NY) capable of handling a voltage up to 500 V. The tuning and matching can, to some extent, be adapted by inflating or deflating the balloon of the endorectal coil. A coaxial cable connected the RF-coil to a home-built TxRx switch with an integrated small band low noise preamplifier (Advanced Receiver Research, Burlington, CT). The TxRx switch was used to interface the coil to a 7-T whole-body MR system (MAGNETOM, Siemens Healthcare, Erlangen, Germany). Figure 1a shows the electronics circuit of the ^{31}P RF-coil.

The forward and reflected power in the ^{31}P transmit channel are monitored by the RF supervision provided

by the manufacturer of the MR system. To determine the reference voltage of the coil, the endorectal coil was placed on a phantom containing Pi. A ^{31}P MRSI pulse-acquire sequence with a 1-ms block pulse was played out at different power levels to estimate the reference power for a flip angle of 180° ($\equiv \gamma B_1 = 500$ Hz) at a distance of 2.5 cm of the center of the coil, which is the distance between the coil and the center of the prostate in vivo. The resulting spectra were analyzed for a dip in the intensity of Pi at this distance.

Eight-Channel ^{1}H TxRx Array Coil

The eight-channel ^{1}H TxRx coil for imaging (16) consists of two arrays with four microstrip line elements, each with meanders (17). Each element has a length of 25 cm, a width of 10 cm, and a thickness of 2 cm. The arrays are placed dorsally and ventrally to the body. The elements of the dorsal array are arranged on a planar sliding frame inside a polymethylmethacrylate housing. The sliding frame is used to place the array at the desired position along the longitudinal axis of the patient. Including a thin cushion for patient comfort, the distance from the elements to the body surface is 25 mm. The elements of the ventral array are enclosed in individual modules made of polycarbonate. The modules are interconnected with a neoprene sheet making the ventral array flexible, so that it can be accommodated to the patient's contour. The distance between the elements and the body is 30 mm, as determined by the module dimensions. Low input impedance preamplifiers and TxRx switches are placed in a separate multipurpose box at the head of the patient table, and the cable length was chosen accordingly to achieve preamp decoupling during reception.

RF Shimming System

^{1}H MR imaging was performed with an add-on system for RF shimming (18), which was integrated into the 7-T MR system and the flexible eight-channel array coil. The RF amplifier of the standard system consists of eight individual modules providing a maximum peak power of 1 kW each (LPPA 13080W, Dressler, Germany) with which the eight-channel RF shimming setup was realized. Computer-controlled attenuators and phase shifters were inserted into the low-power RF chain directly at the input ports of the amplifier. The eight-channel mode is activated by coaxial relays (CX600N, Tohtsu, Japan) connected to the output ports of the RF amplifiers, which bypass the power combiner and power monitor of the standard system and make the eight individual channels available at the patient table.

Unlike the ^{31}P transmit channel, the monitoring of the eight ^{1}H transmit channels cannot be performed by the single channel manufacturer's supervision system. Therefore, a custom-built on-line RF supervision was realized by the use of three logarithmic root-mean-square power meters (TALES, Siemens Healthcare, Erlangen, Germany) which monitor forward and reflected power in the eight transmit channels via directional couplers (19). A real-time field programmable gate array (NI PXI 7852 R, National Instruments, Austin, TX) with corresponding software performed time-averaging of the transmitted RF power over intervals of 10 s and 6 min according to the IEC safety guidelines (15). The correlation between transmit power and localized SAR was determined by RF simulations that are described below. If the maximum permissible input power was exceeded, the software immediately blanked the RF power by emergency relays located in the vector modulator circuit. The monitoring software further included test loops for malfunction detection of the attenuators and phase shifters, and thus correct adjustment of the target RF shim was checked.

In vivo B_1^+ mapping was performed with a protocol based on a presaturation single-shot turboFLASH sequence provided by the vendor of the MR system (20). Relative B_1^+ magnitude and relative phase maps of a single slice were acquired in vivo by low flip angle (estimated below 10°) imaging with a echo time of 5 ms and a repetition time (TR) of 1 s from each coil without presaturation [field of view (FOV) 300 × 300 mm, in plane resolution 4.7 × 4.7 mm, slice thickness 8 mm]. The total acquisition time was 8 s. For the phase maps, the first channel was taken as reference. Thus, the argument of the complex signal ratio between an individual channel and the first channel gives the relative phase. To obtain relative B_1^+ magnitude maps, the individual maps are normalized to the square root of the sum of squares of all individual maps. The relative B_1^+ maps were imported into a graphical user interface that allows the selection of a region of interest (ROI) in the prostate. A RF shimming algorithm was applied that maximizes the magnitude of the B_1^+ distribution inside the ROI by optimizing the transmit phase of the channels while maintaining equal amplitudes. After the desired shim is determined, the vector modulators are automatically programmed with the corresponding phase settings by the control computer. The whole RF shimming procedure including data acquisition, ROI selection, and calculation of the optimal phases takes ~3 min. The flip angle map of the prostate-optimized RF shim was obtained by two images acquired with and without a saturation pulse before the turboFLASH sequence. The cosine of the flip angle produced by the saturation pulse can be approximated by the signal ratio of the presaturated image and the reference image without saturation with the same echo time, TR, total acquisition time, FOV, and resolution as for the relative maps. The flip angle map of the prostate-optimized RF shim was used for transmitter adjustment.

Safety of the Coil Setups

Safety Validation of the ^{31}P Endorectal Coil

FIT simulations, phantom studies, and in vivo measurements were performed to test the safety of the use of the ^{31}P endorectal coil. Numerical computations (CST Studio Suite 2011, Darmstadt, Germany) of the RF field distribution and the corresponding SAR produced by the ^{31}P endorectal coil were performed according to previously presented safety tests for a ^{1}H TxRx endorectal coil (21,22). For the simulation, a detailed computer-aided design model of the coil and the surrounding tissues

(prostate, bladder, muscles, and lipids) was derived (Fig. 3a). The dimensions of the prostate were determined from high-resolution MR images of the human prostate obtained at 3 T. Permittivity and electric conductivity of the tissues at 120.3 MHz were taken from literature (23), and the transverse electromagnetic wave of the coaxial cable was used for RF field excitation at the connector of the cable. The feed point of the loop coil consisting of a small printed circuit board with three capacitors and the connections to the inner and outer conductor of the coaxial cable was modeled as exactly as possible, because it is expected that a high local SAR will be generated in the region of the feed point. With the simulation, we determined the maximum input power to comply with the maximum 10 g averaged SAR (SAR_{10g}) of 10 W/kg. The input power is defined in this study as the difference between forward and reflected power at the table plug. As the simulations provide the input power at the excitation port of the model, we assumed a loss of 1 dB between the table plug to the connecter at the cable of the coil in the simulations to be able to compare results.

To validate that the SAR_{10g} does not underestimate the RF exposure, transient thermal simulations were also performed. For this, the well-known bioheat-transfer equation by Pennes (24), implemented in the simulation software, was utilized. The thermal parameters (heat capacity, thermal conductivity, metabolism, and blood perfusion) of the tissues in the model were taken from parameter sets provided with available heterogeneous body models (25). The heat source for the temperature simulation is given by the power losses in the tissue calculated previously in the RF field simulation. By use of the simulation, the time-averaged input power was determined at which a maximum local temperature of 39°C, specified in the guidelines, was reached after a scan duration of 15 min.

The location of the highest power deposition obtained by the RF simulations was verified in a phantom by MR temperature mapping. A phantom was used as in vivo MR temperature mapping is difficult to perform in the pelvis. A gel phantom was designed with approximately the same dielectric properties as abdominal human tissue (23). A 2% cellulose phantom gel was made using a mixture of isopropanol (52%) and water (48%; Ref. 26). Before dissolving the cellulose, the liquid mixture was buffered with Na_2HPO_4 and NaH_2PO_4 to pH = 7. Sodium chloride (335 mM) was added to obtain a representative conductivity, taking into account the decreasing effect on the conductivity of cellulose and a phantom temperature of 5°C for a high viscosity of the gel (27). The phantom had the following dimensions: 22.5 × 15 × 11.5 cm^3. The relative permittivity and conductivity of the phantom were measured and were 45 and 0.8 S/m, respectively. The ^{31}P endorectal coil was placed in the phantom, and the eight-channel array coil was positioned around it. RF shimming was performed to minimize the effect of B_1 inhomogeneities on the temperature measurements.

To measure the temperature increase with MR thermometry, phase images, acquired with a standard gradient echo sequence, were obtained with the eight-channel array coil before and after transmitting excessive RF power at 120.3 MHz for 2 min with the ^{31}P endorectal coil. Due to the limited sensitivity of the MR thermometry method, an arbitrary high time-averaged input power of 9.1 W was used to acquire adequate phase images. Using the phase images, the temperature change in three slices of 2 mm perpendicular to the coil was calculated (28). The center slice was placed through the feeding point and top of the coil, at the location with the highest predicted SAR deposition according to the simulations. A echo time of 17 ms was used and the in-plane resolution was 2 × 2 mm^2. For MR temperature map validation, three fiber optic temperature sensors of the Luxtron FOT Lab Kit (LumaSense Technologies, Santa Clara, CA) were fixed on the ^{31}P endorectal coil. The sensors were placed close to the feed point, the top of the coil, and on the coil wire as indicated in Fig. 1b, measuring the temperature before, during, and after RF transmission.

The fiber optic temperature sensors were also used for in vivo temperature measurements at the previously determined locations of the highest temperature increase. Thus, the influence of the active thermal regulatory system (e.g., increasing blood perfusion with temperature) on the RF induced temperature elevation could be taken into account. The thermal regulatory system cannot be modeled by simulation. The outer balloon with two temperature sensors was enveloped in a thin condom. It was expected that the insulating effects of the thin latex layer were minimal, and therefore, these were neglected. Next, measurements with increasing power settings were performed to determine the input power that resulted in maximal 1°C temperature increase during a 15-min ^{31}P MRSI measurement. This limit was chosen to assure that a maximum absolute temperature of 39°C is not exceeded in vivo, independent of the state of health of the individual volunteer.

Safety Validation of the Combined Setup of the ^{31}P Endorectal Coil and Eight-Channel ^{1}H Array Coil

The coupling of the eight-channel ^{1}H array coil with the ^{31}P endorectal coil was assessed by simulations and verified in phantom measurements. The simulations were performed with a heterogeneous body model of a 70-kg male (25) in which the prostate, rectum, muscles, fat, and bones of the lower abdomen were modeled with a spatial resolution of 2 mm. The simulations were performed with and without the previously described model of the endorectal coil at a realistic position aligned to the prostate in the heterogeneous body model. For the eight-channel array coil, a computer-aided design-based model was derived from the exact geometries of the implemented coil design. Further, the MR environment with gradient shield, bore cover, and patient table was considered in the model. Dielectric losses from all materials were taken into account. Using a network cosimulation the matching and tuning network, the feed cables, as well as the balanced–unbalanced transformer realized by a coax cable of a half wavelength, inserted at the feed point of every coil element, were considered including losses in the network components. At both transmit frequencies, 120.3 MHz for the ^{31}P endorectal coil, and 297.2 MHz for the eight-channel ^{1}H array coil, the

coupling of the coil ports was monitored, and a possible perturbation of the transmit fields due to the presence of the coil for the other nucleus was analyzed. Furthermore, it was evaluated whether relevant elevations of the local B_1^+ field and SAR distribution generated by the eight-channel array coil occurred close to the ^{31}P endorectal coil that would indicate RF coupling between the different coils. For the calculation of the power-loss density produced by the ^{1}H array coil inside the body, the phase settings for the applied RF shim in the volunteer were used, and the corresponding SAR could be evaluated. Here, the RF shim for the healthy volunteer enrolled in the in vivo ^{31}P MRSI measurement was utilized. The volunteer's body physique agreed well with the body model. The SAR findings were additionally confirmed by transient thermal simulations in the human body model.

The ^{31}P endorectal coil was placed in the above-mentioned gel phantom. On both sides of the phantom, a bottle with the same conductivity and relative permittivity was placed to approximate the loading of a human body in the eight-channel array coil, which was placed around the three phantoms. Using the eight-channel array coil, B_0 and RF shimming of a prostate-sized volume in the phantom gel were performed. Next, a B_1^+ map was acquired using an Actual Flip Angle Imaging sequence (29,30). This gradient echo sequence makes use of two TRs (20 and 100 ms) and one echo time of 2.04 ms and produces a 3D B_1^+ map of the transmitted RF power in the phantom. The resolution was $5 \times 3 \times 3$ mm^3. As the B_1^+ map does not provide information about the electric fields, which can induce heating of the patient, the spatial distribution of the local temperature increase was measured as well. To this end, a relatively high time-averaged RF power of 58 W (intentionally inducing heating in the phantom) was transmitted with the eight-channel array coil for 2 min. Temperature difference maps were calculated as described in the previous section. The temperature was simultaneously measured with the fiber optic temperature sensors (Fig. 1b).

Measurement Protocol

^{31}P RF Excitation Pulse

For 3D ^{31}P MRSI, a pulse-acquire sequence was used with an 8-ms adiabatic excitation BIR-4 pulse with a flip angle of 45° (Fig. 2a). The phase roll, induced by the small delay (0.42 ms) between excitation and start of signal reception to accommodate the phase encode gradients, was removed by first-order phase correction. The adiabatic condition and bandwidth of the RF pulse (Fig. 2b,c) were calculated using the Bloch equations in NMRSIM™ (part of Topspin, Bruker BioSpin Corporation, Billerica, MA).

In Vivo ^{31}P MRSI Measurement

The institutional review board gave approval to perform the in vivo measurements on a volunteer, and signed informed consent was obtained. The ^{31}P endorectal coil was positioned close to the prostate in the rectum of a healthy volunteer. To inflate the inner balloon of the coil, inert perfluoro-polyether liquid (Fomblin, Solvay Solexis, Bollate, Italy) was used. The use of perfluoropolyether minimizes susceptibility differences between the endorectal coil and the tissue, which is a prerequisite for adequate B_0 shimming. The volunteer was placed in supine position on the dorsal array of the eight-channel array coil. The ventral array was fixed over the lower abdomen. To check the matching and loading of the ^{31}P coil and the individual elements of the ^{1}H array coil, power reflection measurements (S_{11}) were performed. The coupling between the coils was assessed by determining the decoupling between the endorectal coil and each element of the array coil at the frequencies of 120.25 and 297.05 MHz. An intramuscular injection of Butylscopolaminebromide (Buscopan, Boehringer-Ingelheim, Ingelheim, Germany) was used to suppress peristalsis.

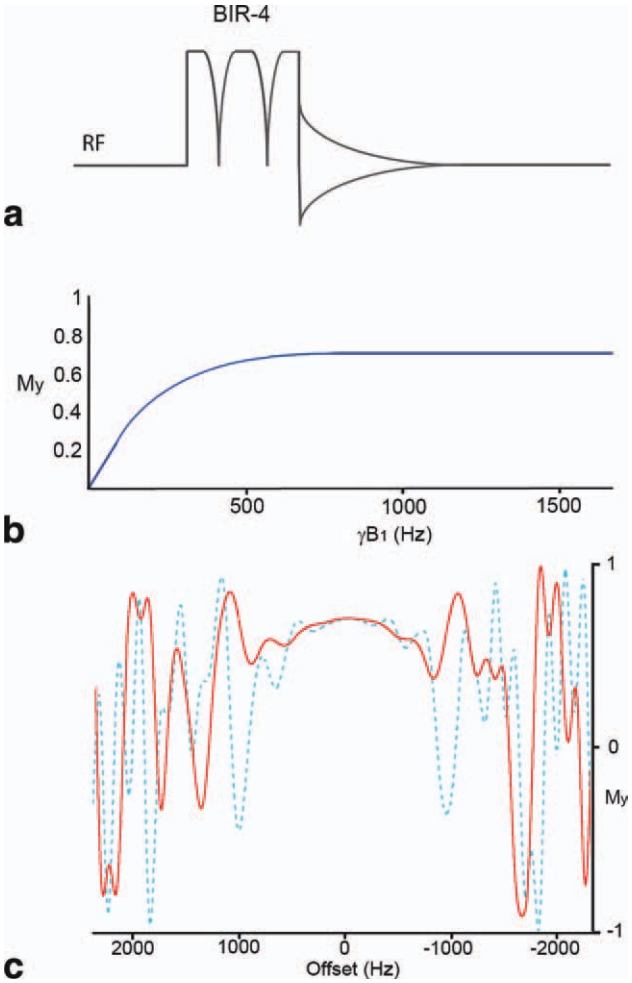

FIG. 2. **a:** Pulse-acquire sequence with a BIR-4 pulse for excitation of the free induction decay. A delay of 0.42 ms between the end of the BIR-4 pulse and start of data acquisition accommodates phase encode gradients in three directions (not shown). **b:** The RF field profile illustrates that the adiabatic condition is met at a γB_1 of 700 Hz and higher. The on-resonance transverse magnetization is 0.71, corresponding to a flip angle of 45°. **c:** Excitation profile at a γB_1 of 933 Hz (solid red) and 700 Hz (dashed blue) resulting in an excitation bandwidth of ~1.5 kHz and 1 kHz, respectively. [Color figure can be viewed in the online issue, which is available at wileyonlinelibrary.com.]

Table 1
The Different Input Powers for the Three Coil Setups and the Reason for Their Use

Coil setup	Input power (W)	
^{31}P TxRx endorectal coil	0.95	Reason: power leading to a maximum 10 g averaged SAR of 10 W/kg Method: derived from RF (SAR) simulations
	1.3	Reason: power leading to a maximum local temperature of 39°C Method: derived from thermal simulations
	9.1	Reason: arbitrary high power for sufficient temperature increase Method: phantom temperature mapping for SAR simulation validation
	1.9	Reason: power leading to a temperature increase in vivo of 1°C Method: in vivo measurement with temperature probes
^{1}H TxRx eight-channel array coil	33	Reason: power leading to a maximum 10 g averaged SAR of 10 W/kg Method: derived from RF (SAR) simulations
Combined ^{31}P TxRx endorectal coil and ^{1}H TxRx eight-channel array coil	33	Reason: power leading to a maximum 10 g averaged SAR of 10 W/kg Method: derived from RF (SAR) simulations
	58	Reason: arbitrary high power for sufficient temperature increase Method: phantom temperature mapping for SAR simulation validation

Fast gradient echo MR sequences were used to check the position of both the ^{31}P endorectal coil and the eight-channel array coil. RF shimming was performed to obtain maximal B_1^+ coherence at the position of the prostate. For anatomical information, six transversal T_2-weighted images of the prostate were acquired using an echo time of 71 ms and a TR of 3000 ms. 3D phasemap shimming was applied to optimize the B_0 homogeneity at the prostate's position. For ^{31}P MRSI, the full FOV of the endorectal coil was spatially encoded (FOV 100 × 100 × 100 mm, matrix of 8 × 8 × 8, 15 averages). The acquisition bandwidth was set to 5000 Hz. The nominal voxel size was 12.5 × 12.5 × 12.5 mm, which resulted in an effective voxel volume of 5.8 cm^3 after apodization of the *k*-space weighted sampling (TR 1.5 s, acquisition time 11 min). In a second measurement, the nominal voxel size was decreased to 11 × 11 × 11 mm^3 (FOV 110 × 110 × 110 mm, matrix of 10 × 10 × 10, 10 averages), representing an effective voxel volume of 4.0 cm^3 (acquisition time 18 min).

With the combination of a TR of 1.5 s and an excitation angle of 45°, we expected limited saturation of the phosphorus metabolites, as estimated T_1 relaxation times at 2 T ranged from 1.1 s (PCr) to 2.6 s (PME) (9), which are not reported to increase when moving to 7 T [no clear field strength dependence has been established (31)].

RESULTS

When validating compliance of a coil setup with either SAR guidelines or temperature limits with different models and measurements, quite a few different input powers need to be reported in this section. Therefore, an overview of the different input powers for three coil setups is given in Table 1 along with a short reason why this input power is reported later.

^{31}P Endorectal Coil and Eight-Channel ^{1}H Array Coil

The reflection coefficient (S_{11}) of the ^{31}P TxRx endorectal coil was −9 dB during use in the phantom and −16 dB during in vivo use at the ^{31}P operating frequency of 120.25 MHz. The unloaded *Q*-factor of the endorectal coil was 316 and the loaded *Q*-factor during in vivo use was 34. The reference voltage of the ^{31}P coil at a distance of 2.5 cm of the center of the coil to attain $\gamma B_1 = 500$ Hz ($\equiv 29$ μT) was 75 V.

The average S_{11} of the eight elements of the eight-channel array coil was −14.8 dB (range −9 to −22 dB).

Safety Validation of the ^{31}P Endorectal Coil

The RF simulations showed that a time-averaged input power of 0.95 W led to a maximum SAR_{10g} of 10 W/kg (Fig. 3b, Table 1). The transient thermal simulations showed that a time-averaged input power of 1.3 W led to a maximum local temperature of 39°C after a scan duration of 15 min (Fig. 3c,e). The calculated S_{11} in the model was −8.7 dB at the frequency of 120.3 MHz.

Figure 3d illustrates the temperature increase in the phantom after 2 min exposure to 9.1 W time-averaged input power with the ^{31}P endorectal coil. There was good agreement between the SAR profile of the simulations (Fig. 3b) and the temperature profile around the coil loop (Fig. 3d). A maximum temperature increase of 3°C was observed near the top and feed point of the coil.

In the in vivo temperature measurements, a time-averaged input power of 1.9 W for the duration of 15 min resulted in a temperature increase of just below 1°C, well below the IEC limit of 39°C during the entire examination (Fig. 3e).

Safety Validation of the Combined Setup of the ^{31}P Endorectal Coil and Eight-Channel ^{1}H Array Coil

The FIT simulations predicted that both coils at both operating frequencies were well decoupled by at least −50 dB. The influence of the endorectal coil on the B_1^+ distribution of the eight-channel array coil was negligible (Fig. 4a,b). Furthermore, the simulation showed that the RF shim concentrated the B_1^+ in the region of the prostate. The highest SAR was located close to the individual elements, and the maximum SAR_{10g}, using in vivo prostate RF shim settings, was close to the upper left coil element of the ^{1}H array coil (Fig. 4c,d). The maximum permissible time-averaged input power of the eight-channel array coil at which the safety limit for the localized

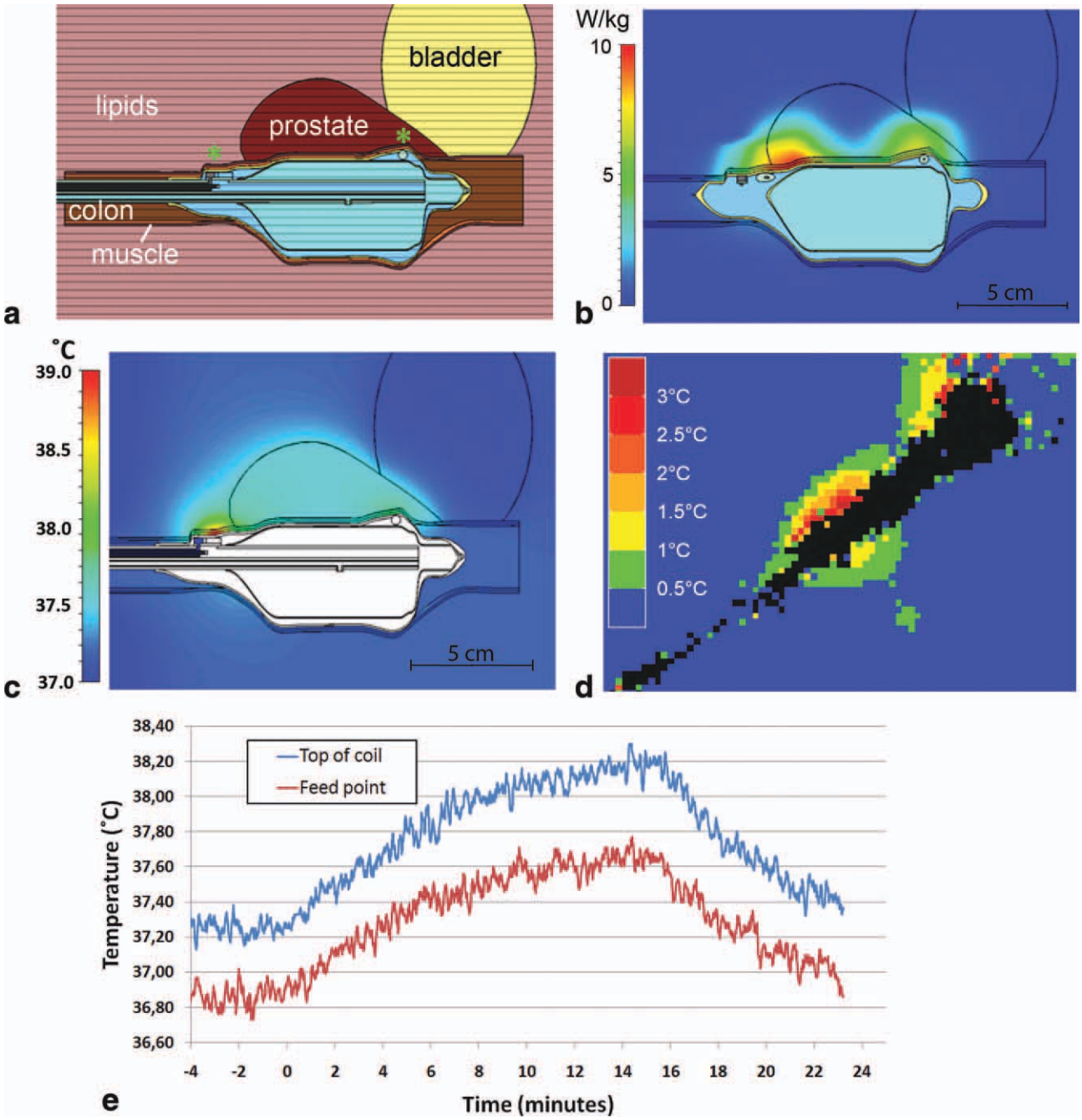

FIG. 3. Safety validation of the ^{31}P endorectal coil. **a:** Finite integration technique simulation model of the endorectal ^{31}P coil, rectum, bladder, and prostate. Two muscles each lateral of the prostate are not shown. **b:** Calculated 10 g averaged SAR using the model in (a) at an RF input power of the ^{31}P endorectal coil of 0.95 W leading to a maximum 10 W/kg assuming a worst case approximation of close contact of tissue and RF-feed without any gap. **c:** Transient thermal simulations after a scan duration of 15 min at a time-averaged input power of 1.3 W leading to a maximum temperature of 39°C. **d:** Image of the temperature increase measured by MR-thermometry after 2 min of 9.1 W of time-averaged input power with the ^{31}P endorectal coil in a phantom. The endorectal coil is rotated 45° counterclockwise in plane compared to the orientation in a, b, and c. **e:** The temperature measured in vivo with fiber optic temperature sensors at the top of the coil and at the feed point during a 15-min ^{31}P MR spectroscopy measurement with the endorectal coil at an input power of 1.9 W. The temperature offset of the two sensors is due to small calibration differences. The location of the fiber optic sensors is shown in (a) with two green asterisks (left: feed point, right: top of the coil).

SAR_{10g} of 10 W/kg was not exceeded was 33W (Fig. 4c,d). There was no relevant SAR elevation close to the endorectal coil, which indicates that the combination of both coils could be operated under safe conditions. This was further supported by the temperature simulations (Fig. 4e,f), which also showed no difference in temperature distribution with and without the endorectal coil after a 15-min experiment for an input power of 33 W.

The absolute B_1^+ map (Fig. 5b) showed the flip angle distribution over the phantom. The RF shimming

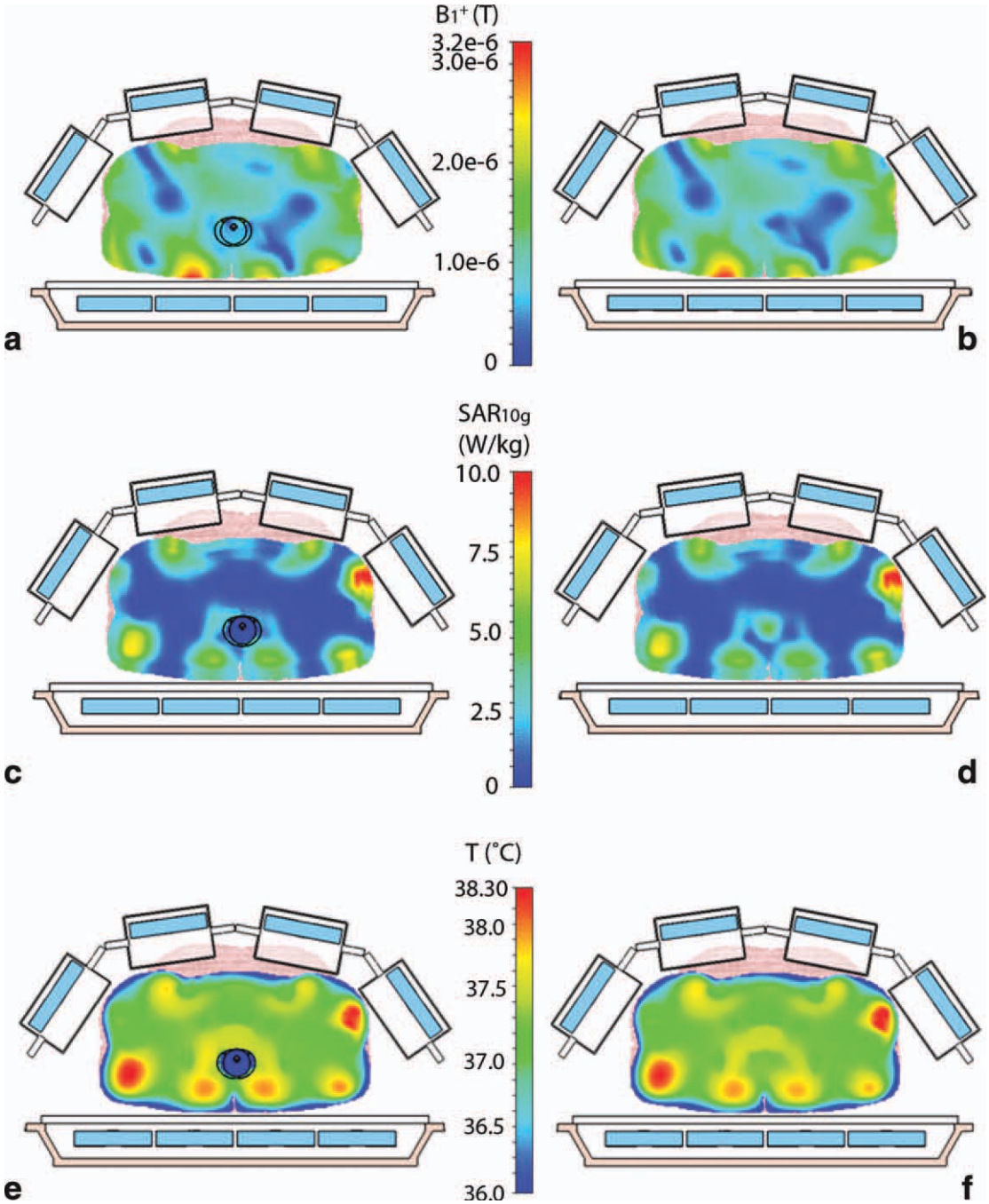

FIG. 4. FIT simulations of the lower abdomen surrounded by the eight elements of the ^{1}H array coil. For the simulations a RF shim maximizing the B_1^+ coherence in the prostate is used. **a:** B_1^+ distribution (in T) at an input power of 33 W of the ^{1}H array coil with the endorectal coil present. **b:** B_1^+ distribution as in (a) but without the endorectal coil. **c:** 10 g averaged SAR (W/kg) distribution at an input power of 33 W of the ^{1}H array coil with the endorectal coil present. **d:** 10 g averaged SAR as in (c) but without the endorectal coil. **e:** Temperature distribution (°C) after a scan duration of 15 min at a time-averaged input power of 33 W of the ^{1}H array coil with the endorectal coil present. **f:** Temperature distribution as in (e) but without the endorectal coil. The location of the prostate is just above the endorectal coil.

method worked well and resulted in maximized B_1^+ at the desired location (Fig. 5b). No B_1^+ elevation was visible near the coil wire. The MR temperature map after 2 min of excessive RF power transmission of 58 W with the eight-channel ^{1}H array coil showed an increase at the top and bottom of the phantom, near the elements of the eight-channel coil but not close to the endorectal coil-loop or the coil-wire (Fig. 5c). The temperature increase measured with the fiber optic temperature sensors was 1.3, 0.5, and 0.5°C at the top, feed point, and wire of the endorectal coil, respectively (Fig. 5d). The sensor at the top of the coil was closest to the dorsal elements of the ^{1}H array coil.

The decoupling between the ^{31}P endorectal coil and each individual element of the eight-channel ^{1}H array coil during in vivo use was on average −71 dB (range

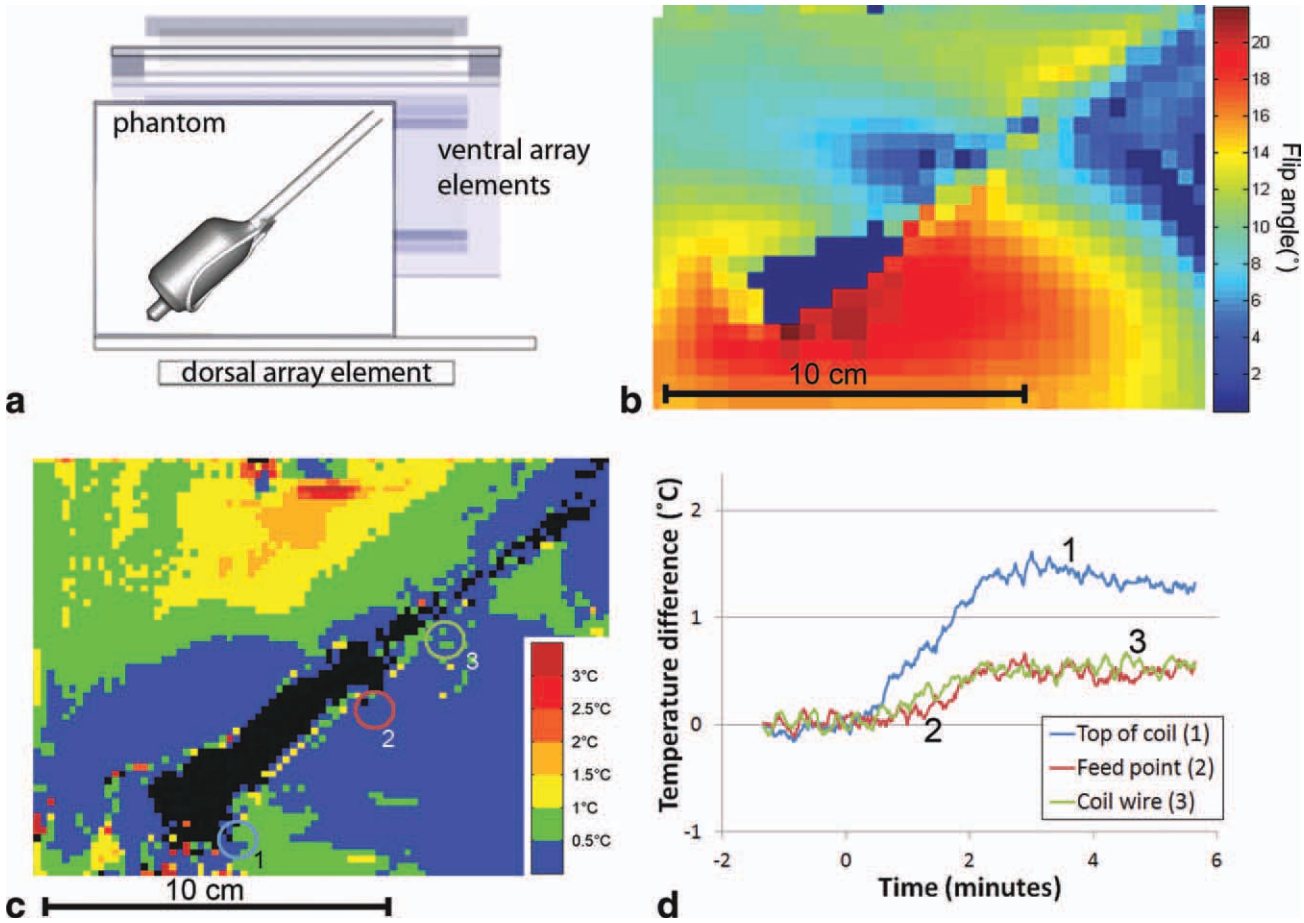

FIG. 5. Phantom study to investigate the presence of coupling between ^{31}P endorectal coil and eight-channel ^{1}H array coil. **a:** Sagittal 3D orientation of the coils and the phantom. The 2D planes in (**b**) and (**c**) are of this sagittal planes. b: Absolute B_1^+ map using the eight-channel array coil showing the flip angle distribution. RF shimming was used to obtain maximal B_1^+ coherence in the area representing the location of the prostate, below the endorectal coil loop. c: Temperature map after 2 min of RF power transmission of 58 W with the eight-channel array coil. **d:** The temperature increase measured with the fiber optic temperature sensors placed at the top of the coil (1 in c), feed point (2 in c), and coil wire (3 in c).

−60 to −80 dB) at 120.25 MHz and −70 dB (range −64 to −80 dB) at 297.05 MHz, demonstrating excellent decoupling.

RF Shimming

We reconstructed relative maps of the B_1^+ magnitude for the individual transmit channels of the eight-channel array coil with the endorectal coil inserted into the rectum (Fig. 6a). Though all elements contributed to the central region where the prostate was located, the individual maps were well separated in the outer region. No significant B_1^+ distortions due to the ^{31}P endorectal coil located in the rectum were visible. RF shimming resulted in quite a homogeneous flip angle distribution for the optimized RF shim (Fig. 6b). The achieved standard deviation of the flip angle inside the prostate was ±10%.

^{31}P RF Excitation Pulse

The calculations from the Bloch equations showed that the adiabatic condition for the BIR-4 pulse of 8 ms was met at a γB_1 of 700 Hz and higher (Fig. 2b). The larger γB_1, the larger the excitation bandwidth (Fig. 2c). The maximum permissible time-averaged power of 1.9 W was reached with the 8 ms pulse with a γB_1 of 933 Hz at 2.5 cm of the coil at a TR of 1500 ms, resulting in a homogeneous excitation bandwidth of 1.5 kHz or more within 2.5 cm of the coil conductors (Fig. 2c). This led to an excitation range of 12 ppm at the ^{31}P frequency at 7 T, indicating good excitation in the posterior and middle part of the prostate. The excitation bandwidth in the anterior part was less. The in vivo ^{31}P MRSI experiments were performed with these experimental settings.

In Vivo Measurement

Using the RF shimming algorithm, good image quality in the base, middle, and apex of the prostate was obtained. B_0 shimming of a ROI over the whole prostate resulted in a water line-width at half maximum of 50 Hz (magnitude). The 3D ^{31}P MRSI grid was aligned using fast gradient echo and T_2-weighted images (Fig. 7a). In the prostate, the resonances of PC, PE, Pi, PCr, and γ-, α-, and β-ATP were detectable (Fig. 7b). The intensity of β-ATP was attenuated due to the limited bandwidth of the BIR-4 pulse. From the seminal vesicles, which are at larger

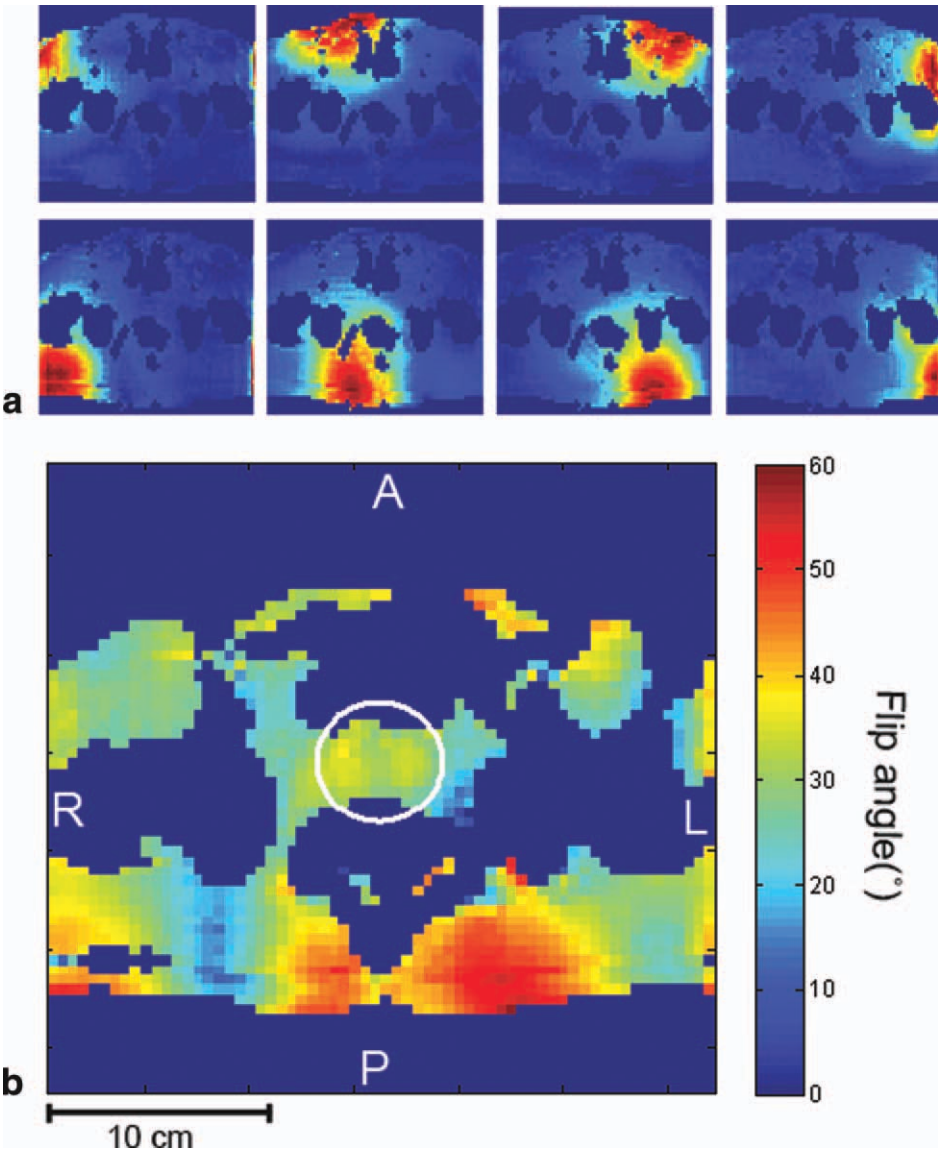

FIG. 6. **a:** In vivo relative maps of the B_1^+ magnitude for the individual transmit channels of the array coil with the endorectal coil inserted into the rectum. **b:** Flip angle distribution for the optimized phase setting of the array coil. Transmit phases were adjusted to obtain maximum B_1^+ inside the prostate (ROI: white circle). The achieved standard deviation of the flip angle inside the ROI is ±10%. [Color figure can be viewed in the online issue, which is available at wileyonlinelibrary.com.]

distance from the center of the coil, good quality spectra were obtained showing an increase in the PC signal (Figs. 7d and 8b). In the surrounding muscles, a high PCr intensity compared to γ- and α-ATP was observed, while in the prostate the intensity of PCr was almost equal to the ATP's (Fig. 7b,c). This could also be demonstrated with a metabolite map of the fitted integral of the PCr signal of the second in vivo measurement obtained with 4 cc voxels (Fig. 8d) and a spatial map of the metabolites in the transversal plane (Fig. 8c). The extent of the transmit field can also be appreciated in this figure.

DISCUSSION

We have demonstrated that our setup for in vivo 3D ^{31}P MRSI of the human prostate at 7 T is feasible for acquisition of these data. For this setup, we combined an eight-channel ^{1}H TxRx array coil and a ^{31}P TxRx endorectal coil to obtain both anatomical information and signals from the phosphorus metabolites. For both coils, the maximum input powers were determined to comply with the IEC 60601-2-33 (Edition 3.0) guidelines, which were a maximum of 10 W/kg for the SAR_{10g} or a maximum local tissue temperature of 39°C.

To ensure that no coupling occurred between the ^{31}P endorectal coil and the eight-channel ^{1}H array coil, simulations and phantom measurements were performed. The FIT simulations showed that the highest SAR_{10g} of the array coil was observed near the ^{1}H elements, with as well as without the endorectal coil present. It was verified by temperature simulations, that the temperature elevation close to the elements of the body coil also exceeded the temperature increase near the endorectal coil. Similar to the SAR evaluation, the temperature distribution was equal with and without the endorectal coil. This was further confirmed by phantom studies showing neither elevated B_1^+ fields nor a temperature increase near the endorectal coil-loop or its wire. In addition, the in vivo coupling between the endorectal coil and each of the ^{1}H elements was below −60 dB, demonstrating excellent decoupling between the coils. With the absence of coupling with the ^{31}P TxRx coil and

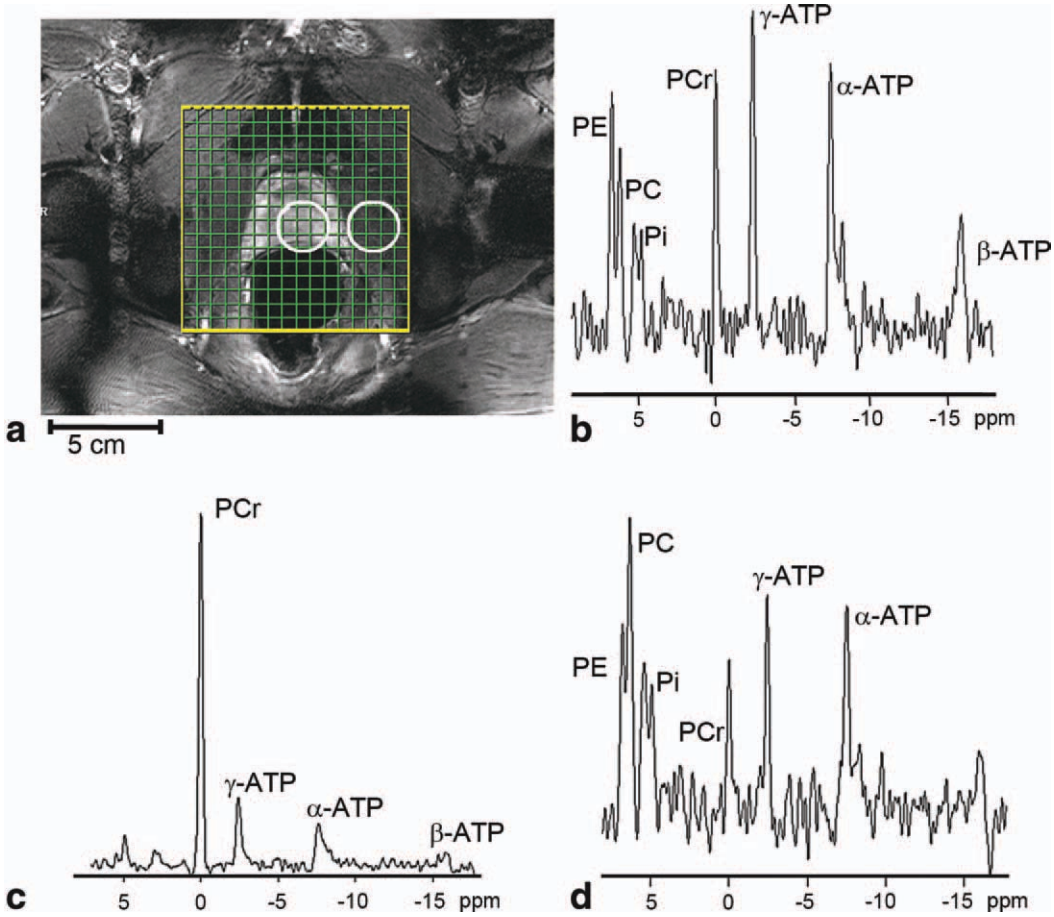

FIG. 7. In vivo ^{31}P MRSI of the prostate at 7 T. **a:** T_2-weighted image of the prostate with one slice of the 3D ^{31}P MR spectroscopy grid. The ^{31}P spectra of 5.8 cm^3 voxels of the prostate (**b**), muscle (**c**), and seminal vesicles (**d**) contain the following metabolites: PCr, Pi, ATP, PE, and PC. The red circles represent the perimeter at 64% of the maximum signal intensity of the spatial response function: best approximation of the true voxel size. The circle in the prostate corresponds to the spectrum in b and the other circle to the muscle spectrum in c. [Color figure can be viewed in the online issue, which is available at wileyonlinelibrary.com.]

the local SAR_{10g} hot-spot close to one of the array elements, we concluded that the presence of the ^{31}P coil does not influence the SAR limitations of use of the ^{1}H body-array coil.

The location of the prostate in the center of the trunk, B_1^+ inhomogeneities, and destructive B_1^+ interferences make it difficult to get enough absolute B_1^+ in the prostate. Therefore, phase modulation of the individual elements is necessary to obtain maximal B_1^+ coherence in the prostate. RF shimming theoretically also enables that a possible perturbation of the B_1^+ distribution of the eight-channel array coil by the endorectal coil can be taken into account during the RF optimization in the prostate. However, no additional B_1^+ perturbations by the endorectal coil were observed in the simulations and phantom studies. Combining the eight-channel array coil and RF shimming system resulted in high-quality anatomical information over the whole prostate and no influence on the image quality in the presence of the coil was seen in vivo.

The maximum permitted RF deposition with the ^{31}P endorectal coil followed from the safety validation. To stay within the SAR_{10g} safety limits, the maximum permitted input power was 0.95 W according to the FIT model simulations of the prostate. The thermal simulations showed that a higher input power of 1.3 W could be used to stay below a local temperature of 39°C. In vivo an even higher power level was possible, because heat can be dissipated by blood flow through the tissue. Limiting the in vivo temperature increase at the hot-spot of the endorectal coil to 1°C during a measurement of 15 min allowed a maximum time-averaged RF power of 1.9 W.

The differences in reported power limits for the ^{31}P endorectal coil can be explained after having a detailed look at the results. The difference in maximum power based on the SAR simulations (0.95 W) and thermal simulations (1.3 W) confirms that the safety limits based on the SAR calculations are conservative and ensure that the temperature limits will not be exceeded. The difference in the SAR and temperature distribution in Fig. 3(b,c) demonstrates the influence of the heat capacity, thermal conductivity, metabolism, and blood perfusion of the tissue on the temperature. When the feed point is close to badly perfused fat tissue, a SAR hot spot results in a larger local temperature increase than the hot spot at the top of the coil inside well-perfused prostate tissue (Fig. 3c): the highest predicted temperature increase is not located within the prostate. Next, there is a difference between the simulations and the power limit

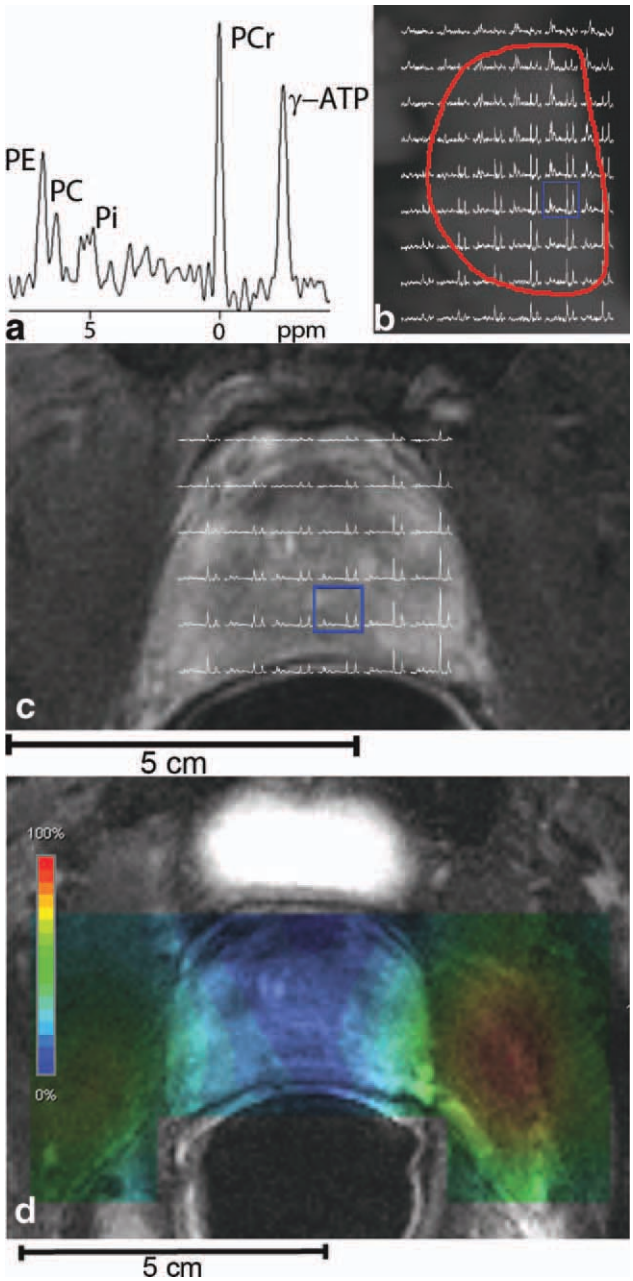

FIG. 8. Spatial maps of the ^{31}P spectra (voxels 5.8 cm^3). **a:** The enlarged spectrum demonstrates the frequency range of the spectra in the transverse (**c**) and sagittal (**b**) planes. The shown metabolites are PE, PC, Pi, PCr, and γ-ATP. The map in the sagittal plane demonstrates the increase in PC signal near the seminal vesicles (upper right region). The signal-to-noise ratios (ratio of the signal integral and standard deviation of the noise) after apodization (20 Hz) of PCr and PE in this spectrum were 163 and 98, respectively. **d:** Metabolite map of the PCr integral of ^{31}P MR spectroscopic imaging (4 cm^3 voxels) placed over a T_2-weighted image of the prostate. The low PCr signals in the prostate are minimally contaminated with the high-PCr signals of the surrounding muscle. [Color figure can be viewed in the online issue, which is available at wileyonlinelibrary.com.]

determined in vivo (1.9 W). The simulations represent a worst case approximation that the tissue and RF-feed are only separated by the latex from the balloon, with no gaps from residual air or glue between the inner and outer balloon. Furthermore, the in vivo measurement also takes into account the active thermal regulatory system (e.g., increase of blood perfusion with temperature), which was not modeled by the bioheat transfer equation in the thermal simulations. Lastly, we cannot be completely sure that the location of the fiber optic temperature sensor is at the exact same location as the location of highest power deposition derived from the simulation. As shown in Fig. 3c, also the position of the coil in the rectum is of importance. The possible differences in actual positioning of the coil and temperature sensors compared to the simulated positioning of these in the model invoked our conservative limit of a maximum 1°C temperature increase during the in vivo measurement.

The SAR limit in our study is based on the normal operating mode of the IEC guideline. In the first level operation mode, the maximum SAR_{10g} limit is 20 W/kg, which would result in an input power of 1.9 W in the RF simulation (twice the simulated input power of 0.95 W compliant with normal operating mode), which incidentally is the same as the power determined with the in vivo temperature measurement.

Following an extensive safety validation, an in vivo experiment was performed. While in previous studies at 1.5 and 2 T in 7–30 min, one single unlocalized spectrum was obtained (8–11), we were able to acquire a complete 3D MRSI dataset in the same time (11–18 min) with accurate localization and relatively high spatial resolution (effective voxel volume down to 4 cm^3). A metabolite map (Fig. 8d) indicated minimal contamination of the low PCr signals in the prostate by the larger PCr signals of the surrounding smooth muscles. The spectra of the different regions in the prostate were of high spectral quality and had a good signal-to-noise ratio (Fig. 7). Also at larger distances from the coil (e.g., in the seminal vesicles and anterior part of the prostate) the spectra contained usable information (Figs. 7d and 8), demonstrating good performance of the coil. An effective voxel volume of 5.6 cm^3 makes it possible to study the different parts (base, midgland, and apex) of the prostate (Fig. 8). As the peripheral zone and central gland in prostate, cancer patients have volumes in the order of 20 cm^3 and larger (32), this resolution also enables detection of metabolic differences between the zones.

Some differences were observed compared to the spectra obtained at 1.5 and 2 T (8–11). First of all, the increase in chemical shift dispersion enabled the separation of PE and PC signals at 7 T. At 1.5 and 2 T, only one peak was visible for PME. In low field studies, also a peak was assigned to PDE, while the spectra in this study are lacking a clear peak for PDE (Fig. 7b,d). Low glycerophosphoethanolamine and glycerophosphocholine levels are reported for prostate tissue in vitro (12,33). The signal-to-noise ratio might be insufficient to detect these peaks in our study. In the Pi region, two or three separate peaks were observed, compared to one peak at lower field strength. What these peaks represent, e.g., compartments with different pH, and how they can be of aid in unraveling metabolic pathways related to prostate cancer should be studied in more detail with more volunteers and patients.

CONCLUSIONS

This study demonstrated that it is safe to combine a ^{31}P TxRx endorectal coil with an eight-channel ^{1}H TxRx body-array coil for prostate imaging and ^{31}P 3D MRSI. The SAR levels of the eight-channel ^{1}H coil were not influenced by the presence of the ^{31}P endorectal coil as was validated by phantom studies, simulations, and in vivo measurements. Furthermore, the maximum time-averaged input power of the ^{31}P endorectal coil was determined. The first in vivo results are promising as high-quality ^{31}P MR spectra were obtained from the whole prostate and surrounding tissues of a healthy volunteer using an effective voxel volume down to 4 cm^3 in an 18-min acquisition. To investigate the value of ^{31}P MRSI at 7 T for the characterization of prostate cancer, an extensive study with prostate cancer patients is required.

REFERENCES

1. Villeirs GM, Oosterlinck W, Vanherreweghe E, De Meerleer GO. A qualitative approach to combined magnetic resonance imaging and spectroscopy in the diagnosis of prostate cancer. Eur J Radiol 2010; 73:352–356.
2. Scheidler J, Hricak H, Vigneron DB, Yu KK, Sokolov DL, Huang LR, Zaloudek CJ, Nelson SJ, Carroll PR, Kurhanewicz J. Prostate cancer: localization with three-dimensional proton MR spectroscopic imaging—clinicopathologic study. Radiology 1999;213:473–480.
3. Fütterer JJ, Heijmink SWTPJ, Scheenen TWJ, Veltman J, Huisman HJ, Vos P, Hulsbergen-Van De Kaa CA, Witjes JA, Krabbe PFM, Heerschap A, Barentsz JO. Prostate cancer localization with dynamic contrast-enhanced MR imaging and proton MR spectroscopic imaging. Radiology 2006;241:449–458.
4. Heerschap A, Jager GJ, Van Der Graaf M, Barentsz JO, De La Rosette JJMCH, Oosterhof GON, Ruijter ETG, Ruijs SHJ. In vivo proton MR spectroscopy reveals altered metabolite content in malignant prostate tissue. Anticancer Res 1997;17:1455–1460.
5. Kurhanewicz J, Vigneron DB, Hricak H, Narayan P, Carroll P, Nelson SJ. Three-dimensional H-1 MR spectroscopic imaging of the in situ human prostate with high (0.24–0.7-cm^3) spatial resolution. Radiology 1996;198:795–805.
6. Scheenen TW, Heijmink SW, Roell SA, Hulsbergen-Van de Kaa CA, Knipscheer BC, Witjes JA, Barentsz JO, Heerschap A. Three-dimensional proton MR spectroscopy of human prostate at 3 T without endorectal coil: feasibility. Radiology 2007;245:507–516.
7. Scheenen TWJ, Fütterer J, Weiland E, Van Hecke P, Lemort M, Zechmann C, Schlemmer HP, Broome D, Villeirs G, Lu J, Barentsz J, Roell S, Heerschap A. Discriminating cancer from noncancer tissue in the prostate by 3-dimensional proton magnetic resonance spectroscopic imaging: a prospective multicenter validation study. Invest Radiol 2011;46:25–33.
8. Kurhanewicz J, Thomas A, Jajodia P, Weiner MW, James TL, Vigneron DB, Narayan P. ^{31}P spectroscopy of the human prostate gland in vivo using a transrectal probe. Magn Reson Med 1991;22: 404–413.
9. Thomas MA, Narayan P, Kurhanewicz J, Jajodia P, James TL, Weiner MW. Detection of phosphorus metabolites in human prostates with a transrectal ^{31}P NMR probe. J Magn Reson 1992;99:377–386.
10. Narayan P, Jajodia P, Kurhanewicz J, Thomas A, MacDonald J, Hubesch B, Hedgcock M, Anderson CM, James TL, Tanagho EA, Weiner M. Characterization of prostate cancer, benign prostatic hyperplasia and normal prostates using transrectal 31phosphorus magnetic resonance spectroscopy: a preliminary report. J Urol 1991; 146:66–74.
11. Hering F, Muller S. ^{31}P MR spectroscopy and ^{1}H MR imaging of the human prostate using a transrectal probe. Urol Res 1991;19:349–352.
12. Komoroski RA, Holder JC, Pappas AA, Finkbeiner AE. ^{31}P NMR of phospholipid metabolites in prostate cancer and benign prostatic hyperplasia. Magn Reson Med 2011;65:911–913.
13. Qiao H, Zhang X, Zhu XH, Du F, Chen W. In vivo ^{31}P MRS of human brain at high/ultrahigh fields: a quantitative comparison of NMR detection sensitivity and spectral resolution between 4 T and 7 T. Magn Reson Med 2006;24:1281–1286.
14. Metzger GJ, Snyder C, Akgun C, Vaughan T, Ugurbil K, Van De Moortele PF. Local B1+ shimming for prostate imaging with transceiver arrays at 7T based on subject-dependent transmit phase measurements. Magn Reson Med 2008;59:396–409.
15. International Electrotechnical Commission—IEC60601–2-33, Edition 3.0, 2010–03: Medical electrical equipment—Part 2–33: particular for the safety of magnetic resonance equipment for medical diagnosis. 2010.
16. Orzada S, Quick HH, Ladd ME, Bahr A, Bolz T, Yazdanbakhsh P, Solbach K, Bitz AK. A Flexible 8-Channel Transmit/Receive Body Coil for 7 T Human Imaging. In: Proceedings of the 17th Annual Meeting of ISMRM, Honolulu, Hawaii, USA, 2009, p 2999.
17. Orzada S, Bahr A, Bolz T.A Novel 7 T Microstrip Element Using Meanders to Enhance Decoupling. In: Proceedings of the 16th Annual Meeting of ISMRM, Toronto, Ontario, Canada, 2008, p 2979.
18. Bitz AK, Brote I, Orzada S, Kraff O, Maderwald S, Quick HH, Yazdanbakhsh P, Solbach K, Bahr A, Bolz T, Wicklow K, Schmitt F, Ladd ME. An 8-Channel Add-On RF Shimming System for Whole-Body 7 Tesla MRI Including Real-Time SAR Monitoring. In: Proceedings of the 17th Annual Meeting of ISMRM, Honolulu, Hawaii, USA, 2009, p 4767.
19. Brote I, Orzada S, Kraff O, Maderwald S, Quick HH, Yazdanbakhsh P, Solbach K, Wicklow K, Bahr A, Bolz T, Ladd ME, Bitz AK. A Multi-channel SAR Prediction and Online Monitoring System at 7 T. In: Proceedings of the 17th Annual Meeting of ISMRM, Honolulu, Hawaii, USA, 2009, p 4788.
20. Fautz HP, Vogel M, Gross P, Kerr A, Zhu Y. B1 Mapping of Coil Arrays for Parallel Transmission. In: Proceedings of the 16th Annual Meeting of ISMRM, Toronto, Ontario, Canada, 2008, p 1247.
21. Klomp DW, Bitz AK, Heerschap A, Scheenen TW. Proton spectroscopic imaging of the human prostate at 7 T. NMR Biomed 2009;22: 495–501.
22. Bitz AK, Klomp DW, Ladd ME. Experimental and Numerical Determination of SAR and Temperature Distribution of a Human Endorectal Coil for MR Imaging of the Prostate at 7 T. In: Proceedings of the 16th Annual Meeting of ISMRM, Toronto, Ontario, Canada, 2008, p 903.
23. Gabriel C. Compilation of the dielectric properties of body tissues at RF and microwave frequencies: Brooks AFB, TX: Brooks AFB, Tech. Rep.; 1996.
24. Pennes HH. Analysis of tissue and arterial blood temperatures in the resting human forearm. J Appl Physiol 1998;85:5–34.
25. Christ A, Kainz W, Hahn EG, Honegger K, Zefferer M, Neufeld E, Rascher W, Janka R, Bautz W, Chen J, Kiefer B, Schmitt P, Hollenbach HP, Shen J, Oberle M, Szczerba D, Kam A, Guag JW, Kuster N. The virtual family—development of surface-based anatomical models of two adults and two children for dosimetric simulations. Phys Med Biol 2010;55:N23–N38.
26. Åkerlöf G. Dielectric constants of some organic solvent–water mixtures at various temperatures. J Am Chem Soc 1932;54:4125–4139.
27. Zhao GQ, Chen SB. Microviscosity of hydrophobically modified hydroxyethyl cellulose aqueous solutions. J Colloid Interf Sci 2008; 322:678–680.
28. Ishihara Y, Calderon A, Watanabe H, Okamoto K, Suzuki Y, Kuroda K, Suzuki Y. A precise and fast temperature mapping using water proton chemical shift. Magn Reson Med 1995;34:814–823.
29. Amadon A, Boulant N. Simultaneous Measurement of B0- And B1-Maps with Modified Actual Flip Angle Imaging Sequence. In: Proceedings of the 16th Annual Meeting of ISMRM, Toronto, Ontario, Canada, 2008.
30. Yarnykh VL. Actual flip-angle imaging in the pulsed steady state: a method for rapid three-dimensional mapping of the transmitted radiofrequency field. Magn Reson Med 2007;57:192–200.
31. Lei H, Zhu XH, Zhang XL, Ugurbil K, Chen W. In vivo ^{31}P magnetic resonance spectroscopy of human brain at 7 T: An initial experience. Magn Reson Med 2003;49:199–205.
32. Zechmann CM, Simpfendörfer T, Giesel FL, Zamecnik P, Thieke C, Hielscher T, Meinzer HP, Delorme S. Comparison of peripheral zone and central gland volume in patients undergoing intensity-modulated radiotherapy. J Comput Assist Tomogr 2010;34:739–745.
33. Swanson MG, Keshari KR, Tabatabai ZL, Simko JP, Shinohara K, Carroll PR, Zektzer AS, Kurhanewicz J. Quantification of choline- and ethanolamine-containing metabolites in human prostate tissues using 1H HR-MAS total correlation spectroscopy. Magn Reson Med 2008; 60:33–40.